PHYSICAL REVIEW B **108**, 045111 (2023)

Multiconfigurational nature of electron correlation within nitrogen vacancy centers in diamond

Yilin Chen,[1] Tonghuan Jiang,[2] Haoxiang Chen,[2] Erxun Han,[2] Ali Alavi,[3,4] Kuang Yu,[5,*]
Enge Wang,[1,6,7,8,†] and Ji Chen[2,6,7,9,‡]
[1]*International Center for Quantum Materials, School of Physics, Peking University, Beijing 100871, People's Republic of China*
[2]*School of Physics, Peking University, Beijing 100871, People's Republic of China*
[3]*Max Planck Institute for Solid State Research, Heisenbergstrasse 1, 70569 Stuttgart, Germany*
[4]*University of Cambridge, Lensfield Road, Cambridge CB2 1EW, United Kingdom*
[5]*Tsinghua-Berkeley Shenzhen Institute (TBSI), Institute of Materials Research (iMR),*
Tsinghua Shenzhen International Graduate School (TSIGS), Tsinghua University, Shenzhen 518055, People's Republic of China
[6]*Interdisciplinary Institute of Light-Element Quantum Materials and Research Center for Light-Element Advanced Materials,*
Peking University, Beijing 100871, People's Republic of China
[7]*Collaborative Innovation Center of Quantum Matter, Beijing 100871, People's Republic of China*
[8]*Songshan Lake Materials Laboratory, Institute of Physics, Chinese Academy of Sciences, Guangdong, People's Republic of China*
[9]*Frontiers Science Center for Nano-Optoelectronics, Peking University, Beijing 100871, People's Republic of China*

(Received 19 October 2022; accepted 23 June 2023; published 10 July 2023)

Diamond is a solid-state platform used to develop quantum technologies, but it has been a long-standing problem that the current understanding of quantum states of nitrogen vacancy (NV) centers in diamond is mostly limited to single-electron pictures. Here, we combine the full configuration interaction quantum Monte Carlo method and the density-matrix functional embedding theory to achieve an accurate description of the many-body quantum states of such defects in diamond. More than 30 electrons and 130 molecular orbitals are correlated, revealing the multiconfigurational nature of the wave functions of the many-body quantum states therein. Such a description explains puzzling experimental measurements in intersystem crossing and charge-state transitions at NV centers in diamond. The calculations not only reproduce the available experimental measurements of the energy gaps between quantum states but also provide benchmarks for states that are still subject to considerable uncertainty.

DOI: 10.1103/PhysRevB.108.045111

I. INTRODUCTION

Diamond is a key component in many quantum technologies such as qubits, photon emitters, and nanosensors, utilizing the isolated and manipulable properties of the quantum states [1,2]. The nitrogen vacancy (NV) centers are systems having such ideal properties, and various applications have already been demonstrated in experiments [3–6]. Although there have been many detailed experimental and theoretical studies on quantum states in diamond from different perspectives, questions remain as to the details of the low-lying spin states and transitions between charge states [7]. The mechanism of intersystem crossing between triplets and dark singlets in the negatively charged NV center (NV^-), a process that is essential for initialization and readout of quantum states, is still controversial [8,9]. A better understanding of the ionization processes of NV centers leading to the neutral (NV^0) and the positively charged (NV^+) states is demanded because the latter states have demonstrated promising applicability in quantum devices [10–12].

Theoretically, the main challenge is to describe the many-electron states in the quantum regime from *ab initio* calculations [7]. The atomic model of an NV center would consist of at least three carbon atoms, one nitrogen atom, and one saturating shell of hydrogen atoms, leading to a demand to correlate more than 30 electrons in hundreds of orbitals. This means that an exact description involves a gigantic number of Slater determinants, i.e., configurations, which are inherently correlated and should be considered on the same footing. Thus far, the most widely accepted physical pictures of the electronic structure of NV centers are often based on mean-field theories, such as Hartree-Fock theory and density functional theory (DFT) [13,14], where only a single configuration is used to approximate the many-electron wave function [15]. Much of the understanding of the NV centers is deeply rooted in such a single-configuration picture, which has led to the successful applications aforementioned. However, in the last few years, deepened theoretical analyses and interpretations of experimental measurements have suggested that correlation effects in diamond are much stronger than anticipated [16–20]; hence establishing a clearer picture of the multiconfigurational nature is desired.

In this paper, we develop a computational framework which allows us to perform full configuration interaction quantum Monte Carlo (FCIQMC) together with a quantum embedding technique, namely, the density-matrix functional

---

[*] yu.kuang@sz.tsinghua.edu.cn
[†] egwang@pku.edu.cn
[‡] ji.chen@pku.edu.cn

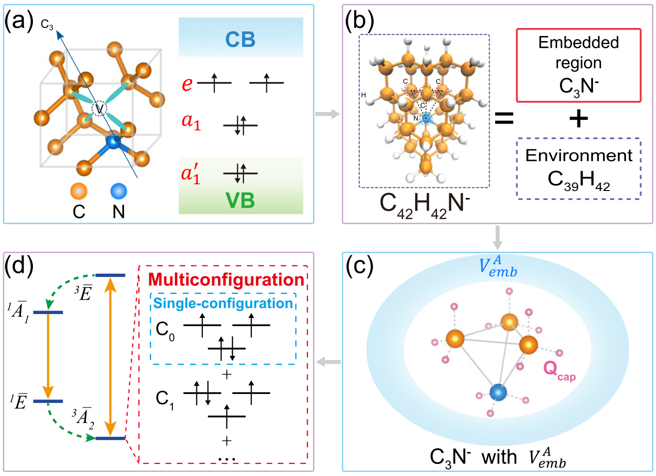

FIG. 1. Flowchart of this work. (a) Left: the local structure of the NV^- center in diamond. Right: a sketch of the single-particle band structure and related states between the valence band (VB) and the conduction band (CB; degenerate $e_{x,y}$, a_1, and a_1'), where the arrows indicate the spin occupations of the ground state. (b) The partitioning scheme of a cluster $C_{42}H_{42}N^-$ containing the NV^- center. (c) A sketch of constructing the DFT embedding potential using DMFET, orbital orthogonalization, and orbital projection. (d) The multiconfigurational electronic structure of the NV^- center. Left: showing four important low-lying states: the ground triplet state $^3\bar{A}_2$, the optical excited triplet state $^3\bar{E}$, and the dark intermediate singlet states $^1\bar{A}_1$ and $^1\bar{E}$. The green dashed arrows highlight the intersystem crossing (ISC) processes $^3\bar{E} \leftrightarrow {}^1\bar{A}_1$ and $^1\bar{E} \leftrightarrow {}^3\bar{A}_2$. Right: the configurations of the ground state $^3\bar{A}_2$. The blue box represents the single-configurational picture, while the red box highlights the strongly correlated multiconfigurational picture obtained by FCIQMC-in-DFT.

embedding theory (DMFET). FCIQMC is a stochastic sampling method that solves the full configuration interaction problem, yielding accurate solutions to the quantum chemical Hamiltonian in a large space of configurations [21–23]. DMFET is a robust quantum embedding scheme accounting for the correlation effects from the outer regimes of the material quantum mechanically [24,25]. Our approach, dubbed FCIQMC-in-DFT, can effectively overcome the difficulties encountered in previous theoretical studies, namely, the simultaneous inclusion of an accurate quantum environment and full correlation at the site of the defect. Using FCIQMC-in-DFT, we establish here a much deeper understanding of the quantum states in NV centers in diamond, highlighting their multiconfigurational nature and the consequent impact on the transition processes between different quantum states.

II. COMPUTATIONAL FRAMEWORK AND METHODS

A. Model of NV centers and computational framework

An overview of the general strategy of FCIQMC-in-DFT calculations is given in Fig. 1. An NV center is a point defect in diamond [left panel of Fig. 1(a)], consisting of a substitutional nitrogen and a vacancy at its nearest-neighbor site with C_{3v} symmetry. The minimum model to describe the electronic structure of NV centers is the four-orbital model. As an example, the right panel of Fig. 1(a) shows a sketch of the single-particle picture of the negatively charged NV center (NV^-), which is the most stable state. The electronic ground state of NV^- includes the degenerate $e_{x,y}$ and the a_1 defect levels, i.e., a one-electron state, in the conduction-band–valence band gap (5.4 eV). In addition, an a_1' orbital is within the valence band, near its top. The arrows show the occupation of the six electrons in the four orbitals of the ground state of NV^- [26]. To distinguish these states from the states within the single-configurational picture (e.g., ^1E), we label the multiconfigurational electronic states with $^1\bar{E}$. For NV^-, the most relevant electronic states are the four low-lying states shown in Fig. 1(d), including the spin triplets ground state $^3\bar{A}_2$ and an optical active excited state $^3\bar{E}$, along with the intermediate spin singlets $^1\bar{A}_1$ and $^1\bar{E}$ [13,14].

It is worth noting that both cluster models and periodic models have been used in embedded calculations reported in the literature. Cluster models and periodic models both have pros and cons. In our case, we focus on NV centers with very low concentrations as they are relevant in single-defect experiments. This causes challenges for the periodic models because large supercell calculations involving thousands of atoms are needed to model the defect; otherwise, the interaction between the periodic images of the defect may lead to significant overestimation of the correlation effects. Cluster models are free of defect-defect interactions, but the size of the cluster could also affect the description of the environmental effects on the defect states. Therefore, before the FCIQMC-in-DFT study is performed, nonembedded calculations are performed to systematically determine suitable settings, such as the size of the cluster, the embedded region, the environment and the exchange correlation functional of DFT and the basis set.

We start the nonembedded calculations with the smallest $C_3H_{12}N^-$ cluster, where we can perform converged FCIQMC benchmark calculations of the low-lying states. The results of other *ab initio* methods are also computed and compared, which highlights the strong correlation nature of all electronic states in NV^-, whereas DFT results strongly depend on the choice of exchange correlation functional. A larger cluster ($C_{15}H_{36}N^-$) is calculated using the coupled-cluster method including up to perturbative triples, namely, the coupled-cluster method with singles and doubles (triples) [CCSD(T)]. DFT calculations are also performed on $C_{15}H_{36}N^-$ as well as larger clusters, $C_{42}H_{42}N^-$ and $C_{163}H_{100}N^-$. These calculations lead to the selection of $C_{42}H_{42}N^-$ for FCIQMC-in-DFT calculations, in which the embedded region is C_3N^-. In addition, we find that the best-performing exchange correlation functional tested is the revised Heyd-Scuseria-Ernzerhof exchange correlation functional HSE06, and it is then used to describe the environment in FCIQMC-in-DFT calculations. See Supplemental Material (SM) [27] for computational details, additional results, and extended discussions, which include additional references [28–32]. A complete description of the nonembedded calculations is given in SM Sec. SII. These tests also provide data to make posterior error corrections of our results, as described in SM Sec. SIII.

With the selected cluster, we start from a common nonlocal embedding potential constructed by DMFET, under which the sum of the subsystem DFT density matrices reproduces the reference density matrix of the total system. Figure 2(a) shows a flowchart for constructing the embedding potential, where

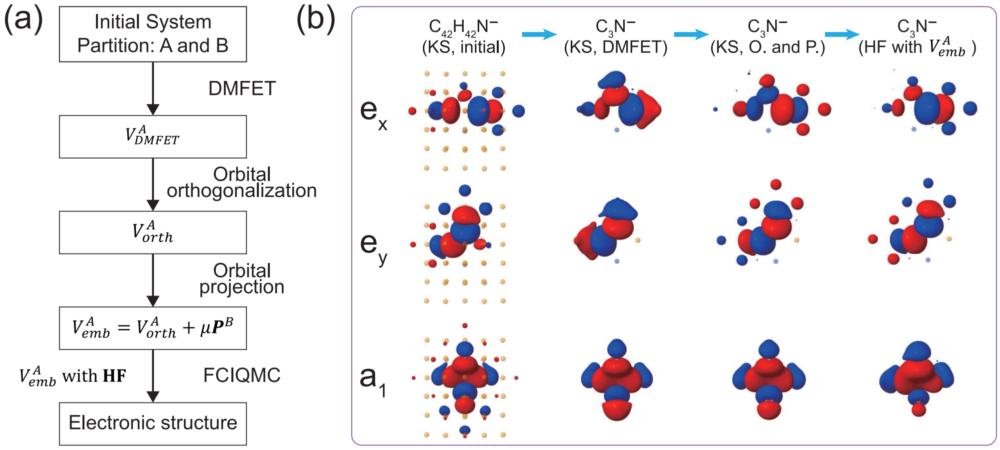

FIG. 2. (a) Flowchart of FCIQMC-in-DFT. (b) Calculated frontier molecular orbitals $e_{x,y}$ and a_1. The translucent orange atoms represent carbon, and blue atoms represent nitrogen. Hydrogen atoms are not plotted. The Kohn-Sham (KS) orbitals are obtained by DFT calculations with the HSE06 exchange correlation functional, 6-31G basis set, and Gaussian smearing. Starting from the initial system $C_{42}H_{42}N^-$, the DFT embedding potential V^A_{emb} of the embedded region C_3N^- is obtained through DMFET, orbital orthogonalization, and orbital projection (O. and P., respectively). Finally, FCIQMC is performed using the restricted Hartree-Fock (HF) orbitals with V^A_{emb} and the 6-31G basis set.

the embedded region (C_3N^-) is labeled as subsystem A and the environment is labeled as subsystem B ($C_{39}H_{42}$). We start from a common nonlocal embedding potential constructed by DMFET, under which the sum of the subsystem DFT density matrices reproduces the reference density matrix of the total system. We follow sequentially a standard DMFET, an orbital orthogonalization, and a level-shifting projection term devised by Manby *et al.* [33], and finally, we get the DFT embedding potential V^A_{emb}, which can describe the interaction effects of the environment on the embedded region [Fig. 1(c)]. Figure 2(b) shows the calculated molecular orbitals $e_{x,y}$ and a_1 of NV^- during the whole process. The subsequent FCIQMC calculations were performed with the restricted Hartree-Fock orbitals of the embedded region C_3N^- and this DFT embedding potential V^A_{emb}.

B. DMFET

Here we employ the density-matrix functional embedding theory (DMFET) developed by Yu and Carter [24] and Zhang and Carter [25]. The main idea of DMFET is to use the DFT one-particle density matrix of the total system as a fitting target. A common nonlocal embedding potential is constructed, under which the sum of the subsystem DFT density matrices reproduces the total reference density matrix.

Specifically, in DMFET, we first perform a DFT calculation on the total system to get the reference one-particle density matrix $D^{\text{ref}}_{\text{tot}}(\vec{r}, \vec{r}\,')$. Then, the total system can be partitioned into two parts, subsystem A (embedded region) with density matrix $D_A(\vec{r}, \vec{r}\,')$ and subsystem B (environment) with density matrix $D_B(\vec{r}, \vec{r}\,')$. In the partition, when we cleave a covalent bond, both bonding electrons will be assigned to the embedded region, with a cation left in the environment. In order to cap the resulting dangling bonds, positive point charges will be placed on the original bonding axis for the embedded region, and negative point charges will be placed on the original bonding axis for the environment. Correspondingly, we denote the electrostatic potential of the positive capping charge as V^A_{cap} and the potential of the negative capping charge as V^B_{cap}. Then a common nonlocal potential $V_{\text{com}}(\vec{r}, \vec{r}\,')$ is applied on both subsystems, and the total embedding potentials for subsystems A and B can be written as

$$\begin{aligned} V^A_{\text{DMFET}} &= V_{\text{com}} + V^A_{\text{cap}} \\ V^B_{\text{DMFET}} &= V_{\text{com}} + V^B_{\text{cap}}. \end{aligned} \tag{1}$$

We then optimize V_{com} such that

$$D^{\text{ref}}_{\text{tot}}(\vec{r}, \vec{r}\,') = D_A\big[V^A_{\text{DMFET}}(\vec{r}, \vec{r}\,')\big] + D_B\big[V^B_{\text{DMFET}}(\vec{r}, \vec{r}\,')\big]. \tag{2}$$

In practice, the optimization is conducted by maximizing the extended Wu-Yang optimized effective potential (OEP) functional:

$$\begin{aligned} W[V_{\text{com}}] = {} & E_A[D_A] + E_B[D_B] \\ & + \int \big(D_A + D_B - D^{\text{ref}}_{\text{tot}}\big) \cdot V_{\text{com}} d\vec{r} d\vec{r}\,', \end{aligned} \tag{3}$$

where D_A and D_B are obtained by DFT calculations of the embedded region and the environment under the embedding potentials V^A_{DMFET} and V^B_{DMFET}, respectively. It has been proven that the derivative of $W[V_{\text{com}}]$ with respect to V_{com} is $(D_A + D_B - D^{\text{ref}}_{\text{tot}})$. So once W reaches its maximum, Eq. (2) is satisfied. The V^A_{DMFET} obtained by Eq. (1) is the DMFET embedding potential needed for the embedded region.

C. Orbital orthogonalization and level-shifting projector

In previous work [24], it is proven that if all density matrices are idempotent (i.e., all orbitals have integer occupancies), the occupied orbitals generated by DMFET are orthogonal between the embedded region and the environment. Such a property is important as it allows implementation of the Manby's projector [33], which enforces the Pauli exclusion principle in the following embedded FCIQMC calculation (*vide infra*). However, during the OEP process, the optimizer may explore embedding potentials with unphysical values, making the subsystem self-consistent field (SCF) iterations unstable. Therefore we often have to apply a Gaussian smearing scheme [34] to stabilize the subsystem SCF convergence, effectively allowing partial occupancy of the frontier orbitals and breaking the orthogonality condition. In our previous study [24], a large smearing width (0.05 E_h) was used as merely a numerical tool to preconverge the OEP calculation. The final embedding potential was still converged with a small smearing width of 0.005 E_h, which has a negligible effect on the integer occupancies of the orbitals. See more details in SM Sec. SIII B. While such a scheme works well for closed-shell systems, in the case of an NV^- center we find the situation to be much more complicated due to the degenerate singly occupied orbitals $e_{x,y}$. In order to retain such degeneracy in a non-spin-polarized single-determinant calculation, a relatively large smearing width is necessary. Consequently, further treatments are required after the original DMFET to enforce the orthogonality between the two subsystems.

We then consider the nonorthogonal orbital subspace, which contains the degenerate $e_{x,y}$ orbitals and the two environment orbitals with obvious fractional occupancies. Numerically, they are the orbitals that show significant overlaps after DMFET ($|C_A^T S C_B|_{ij} > 0.01$). A Löwdin orthogonalization is performed in this subspace, and the orthogonalized orbitals are reassigned to subsystems according to their occupancies. The new degenerate singly occupied orbitals are assigned to the embedded region, while the rest (with double occupancies) are assigned to the environment. The general ideas of this process are presented here, and the detailed procedures are presented in SM Sec. SIII C.

Consider an atomic orbital (AO) basis set $\{\varphi_\mu\}$, with overlap matrix $\mathbf{S}_{\mu\upsilon} = \langle\varphi_\mu|\varphi_\upsilon\rangle$. The relationship between the density and the density matrix is basically

$$\rho(r) = \sum_{\mu\upsilon} \mathbf{D}_{\mu\upsilon}\varphi_\mu^*\varphi_\upsilon. \tag{4}$$

To perform Löwdin orthogonalization, we define the orthogonalized basis set $\{\overline{\varphi}_\mu\}$:

$$\overline{\varphi}_\mu = \mathbf{X}_{\mu\upsilon}\varphi_\upsilon, \tag{5}$$

where

$$\mathbf{X}_{\mu\upsilon} = \mathbf{S}_{\mu\upsilon}^{-1/2}. \tag{6}$$

Obviously, the orthogonalized basis set satisfies

$$\langle\overline{\varphi}_\mu|\overline{\varphi}_\upsilon\rangle = \sum_{\alpha\beta}\mathbf{X}_{\mu\alpha}\mathbf{X}_{\upsilon\beta}\langle\varphi_\alpha|\varphi_\beta\rangle = \mathbf{XSX}^T = \mathbf{I}. \tag{7}$$

Then the density matrix in the orthogonalized basis can be defined considering

$$\begin{aligned}\rho(r) &= \sum_{\alpha\beta}\mathbf{D}_{\alpha\beta}\varphi_\alpha^*\varphi_\beta \\ &= \sum_{\mu\upsilon}\sum_{\alpha\beta}\mathbf{D}_{\alpha\beta}\mathbf{X}_{\alpha\mu}^{-1}\overline{\varphi}_\mu^*\mathbf{X}_{\beta\upsilon}^{-1}\overline{\varphi}_\upsilon \\ &= \sum_{\mu\upsilon}\overline{\mathbf{D}}_{\mu\upsilon}\overline{\varphi}_\mu^*\overline{\varphi}_\upsilon.\end{aligned} \tag{8}$$

With $\mathbf{X}$ being symmetric, the density matrix is orthogonalized as

$$\overline{\mathbf{D}} = \mathbf{X}^{-1}\mathbf{D}\mathbf{X}^{-1}. \tag{9}$$

The orthogonalization leads to two density matrices D_{orth}^A and D_{orth}^B for the embedded region and the environment, respectively. At this point, the embedding potential V_{DMFET}^A obtained in the original DMFET no longer matches the obtained D_{orth}^A. So an additional OEP is conducted for the embedded region, using the original V_{DMFET}^A as the initial guess. Technically, we maximize the following functional, with an L^2 regularization term controlled by prefactor α:

$$W_A\big[V_{\text{orth}}^A\big] = E_A[D_A] + \int\big(D_A - D_{\text{orth}}^A\big)\cdot V_{\text{orth}}^A d\vec{r}d\vec{r}' + \alpha\big\|V_{\text{orth}}^A\big\|^2. \tag{10}$$

One can prove that the derivative of $W_A[V_{\text{orth}}^A]$ with respect to V_{orth}^A is $(D_A - D_{\text{orth}}^A + 2\alpha V_{\text{orth}}^A)$. Considering that α is quite small ($\alpha = 0.001$; see details in SM Sec. SIII D), $D_A = D_{\text{orth}}^A$ is satisfied when V_{orth}^A is an extremum of $W_A[V_{\text{orth}}^A]$. After such an operation, the overlaps between the embedded region and the environment become quite small ($|C_A^T S C_B|_{\max} < 0.01$); thus the orthogonality between the two parts is greatly enhanced.

Using the orthogonalized environment orbitals, we implement the level-shifting projector devised by Manby *et al.* [33] in the following embedded FCIQMC calculations, which was also applied in the previous subspace DMFET work [25]. The environment density matrix after orthogonalization (D_{orth}^B) is used to construct the projection term $\mu\mathbf{P}^B$, where the level-shift parameter μ takes a large positive value ($\mu = 10\,000$; see details in SM Sec. SIII E):

$$\mathbf{P}_{\alpha\beta}^B = \langle\alpha|\left\{\sum_{j\in B}|\phi_j^B\rangle\langle\phi_j^B|\right\}|\beta\rangle = \big[\mathbf{S}D_{\text{orth}}^B\mathbf{S}\big]_{\alpha\beta}, \tag{11}$$

where ϕ_j^B are the occupied Kohn-Sham (KS) orbitals belonging to the environment after orthogonalization and $\mathbf{S}$ is the AO overlap matrix. Such projection penalizes the overlap between the embedded region wave function and the occupied orbitals of the environment and thus enforces Pauli repulsion between the embedded region and the environment during the embedded FCIQMC calculation.

Finally, we get the embedding potential V_{emb}^A for embedded region A:

$$V_{\text{emb}}^A = V_{\text{orth}}^A + \mu\mathbf{P}^B. \tag{12}$$

D. FCIQMC

FCIQMC is a method that uses a stochastic algorithm to solve the full configuration interaction (FCI) [21,22], where the many-body wave function is expanded by a linear combination of all possible configurations in the Hilbert space of a given basis set,

$$\Psi = \sum_i C_i D_i,$$

$$D_i = \frac{1}{\sqrt{N!}}\det\begin{vmatrix}\psi_{i1}(x_1) & \psi_{i2}(x_1) & \cdots & \psi_{iN}(x_1)\\ \psi_{i1}(x_2) & \psi_{i2}(x_2) & \cdots & \psi_{iN}(x_2)\\ \vdots & \vdots & \cdots & \vdots\\ \psi_{i1}(x_N) & \psi_{i2}(x_N) & \cdots & \psi_{iN}(x_N)\end{vmatrix}, \tag{13}$$

where C_i and D_i correspond to the expanding coefficient and the configuration, given by the Slater determinant of single-electron orbitals. N is the total number of electrons. The FCI is considered as the exact solution under the given basis set. In the FCIQMC calculation, the wave function is propagated with Monte Carlo walkers following the master equation of the C_i coefficient,

$$C_i(\tau + \delta\tau) = (1 - \delta\tau(H_{ii} - S))C_i(\tau) - \delta\tau \sum_{j\neq i} H_{ij}C_j(\tau), \tag{14}$$

where H is the Hamiltonian and S is a parameter to be adjusted during the evolution for population control. The ground state of the many-body electronic wave function is reached as the imaginary time evolution proceeds $\tau \to \infty$. The initiator method is used to control the sign problem [35]. This introduces a bias in the sampled wave function which, in the limit of a large number of walkers, tends to zero, leading to near-exact, FCI-quality, solutions. The convergence to the FCI limit is greatly accelerated using the adaptive-shift method [36,37], which is employed in this study.

III. RESULTS AND DISCUSSION

A. Negatively charged NV centers

1. Energies of $^3\bar{A}_2$ and $^1\bar{E}$

With FCIQMC-in-DFT calculations, we first discuss the lowest-energy singlet and triplet states of NV$^-$, namely, the $^1\bar{E}$ and $^3\bar{A}_2$ states. The FCIQMC-in-DFT calculations on the excited states, $^3\bar{E}$ and $^1\bar{A}_1$, are more challenging and will be discussed separately in Sec. III A 3. In Figs. 3(a) and 3(b) we plot the energies of $^1\bar{E}$ and $^3\bar{A}_2$ of NV$^-$ and the excitation energy of $^1\bar{E} \leftrightarrow {}^3\bar{A}_2$, as a function of the total number of walkers in FCIQMC. The vertical excitation energy of $^1\bar{E} \leftrightarrow {}^3\bar{A}_2$ reaches 0.572 eV at 3×10^8 walkers [red dashed line in Fig. 3(b)], within an error of 0.01 eV. Using the nonembedding calculations, we can further estimate the finite-size effect of −0.014 eV, the basis-set effect of −0.004 eV, and the molecular orbital truncation error of +0.029 eV (SM Sec. SV). All the error corrections above only add up to +0.011 eV, which makes very minor changes to our final results. We can then correct the vertical excitation energy to 0.583 eV for $^1\bar{E} \leftrightarrow {}^3\bar{A}_2$ with embedded FCIQMC calculations.

As mentioned above, the transition between the $^1\bar{E}$ state and the $^3\bar{A}_2$ state is an essential intersystem crossing process of NV$^-$, but the gap is still undetermined experimentally. In Table I, we further compare the results of the intersystem crossing energy from different studies using state-of-the-art computational methods. Figure 4 provides a clear and detailed visual representation of the different methods above used to calculate vertical excitation energies (VEEs). The electronic structure methods used in combination with H-terminated cluster models include FCIQMC (this paper), stochastic configuration interaction (CI), DFT, and the Hubbard model. Hedin's *GW* approximation with the Bethe-Salpeter equation (GW+BSE), configuration interaction with constrained random phase approximation (CI-cRPA), and variational quantum eigensolvers (VQEs) are used within periodic models. For $^1\bar{E} \leftrightarrow {}^3\bar{A}_2$ excitation, our calculations agree quantitatively well with all the listed results, with the largest deviation being 0.2 eV. The authors of Ref. [18] employed the stochastic configuration interaction (CI) method to calculate the electronic structures of cluster C_{42} with the same size as FCIQMC-in-DFT, yielding values of 0.629 and 0.644 eV. They also performed DFT calculations on cluster C_{284}, obtaining a value of 0.482 eV. The authors of Ref. [17] utilized a C_{71} cluster in combination with the Hubbard model, producing a result of 0.41 eV. Periodic methods, including GW+BSE in Ref. [16], three CI methods (CI, CI-RPA, and CI-cRPA) in Ref. [19], variational quantum eigensolvers (VQEs) in Refs. [20,39], and an extended Hubbard model fitted to GW in Ref. [9], all generated results within the range 0.5–0.7 eV. In particular, our result is consistent with the stochastic CI calculations of Delaney *et al.* [18], as well as the CI result of Bockstedte *et al.* [19], and the quantum computer simulation results of Ma *et al.* [20]. More precisely, our result is in between their results with a maximum difference of 0.1 eV. It can be observed that both the cluster and periodic models provide consistent descriptions of the excitation energy for $^1\bar{E} \leftrightarrow {}^3\bar{A}_2$.

2. Multiconfigurational nature of $^3\bar{A}_2$ and $^1\bar{E}$

In addition to the excitation energies, more importantly, FCIQMC calculations allow us to establish, without *a priori* assumptions, the composition of the many-electron wave function of quantum states, which is expressed as $\Psi = \sum_i C_i \times D_i$, where D_i is a configuration and C_i is the corresponding expansion coefficient. Figure 1(a) presents the occupation of the reference determinant of the ground state $^3\bar{A}_2$ of NV$^-$. The relevant frontier orbitals, $e_{x,y}$ and a_1, are further plotted in Fig. 3(c). Figure 3(e) shows the configuration graphs of the $^1\bar{E}$ and $^3\bar{A}_2$ states, following the scheme proposed in Ref. [38]. In the graphs, each circle represents a configuration, and the lines characterize the connection between configurations. The size is proportional to the absolute value of the CI coefficient. A shorter line corresponds to a larger transition matrix element, along which FCIQMC spawning is more likely to happen. We can see that both the triplet and singlet states are very multiconfigurational, where the leading four configurations are disconnected from each other. Figure 3(d) plots the population of the top 20 configurations for both the $^3\bar{A}_2$ and $^1\bar{E}$ of NV$^-$. The occupation of the leading configuration is less than 0.3, whereas in a typical system that is not strongly correlated the leading occupation is often larger than 0.9. The multiconfigurational nature highlights the importance of electron correlations in NV centers.

Before further discussion, it is worth mentioning that mean-field theories can be successful for some properties, such as reproducing the parameters experimentally observed in electron paramagnetic resonance (EPR) spectroscopy. Therefore, to further confirm the reliability of our approach, we calculated the spin and magnetization densities of $^3\bar{A}_2$ using both mean-field (embedding potential V^A_{emb} combined with Hartree-Fock orbitals) and multiconfigurational

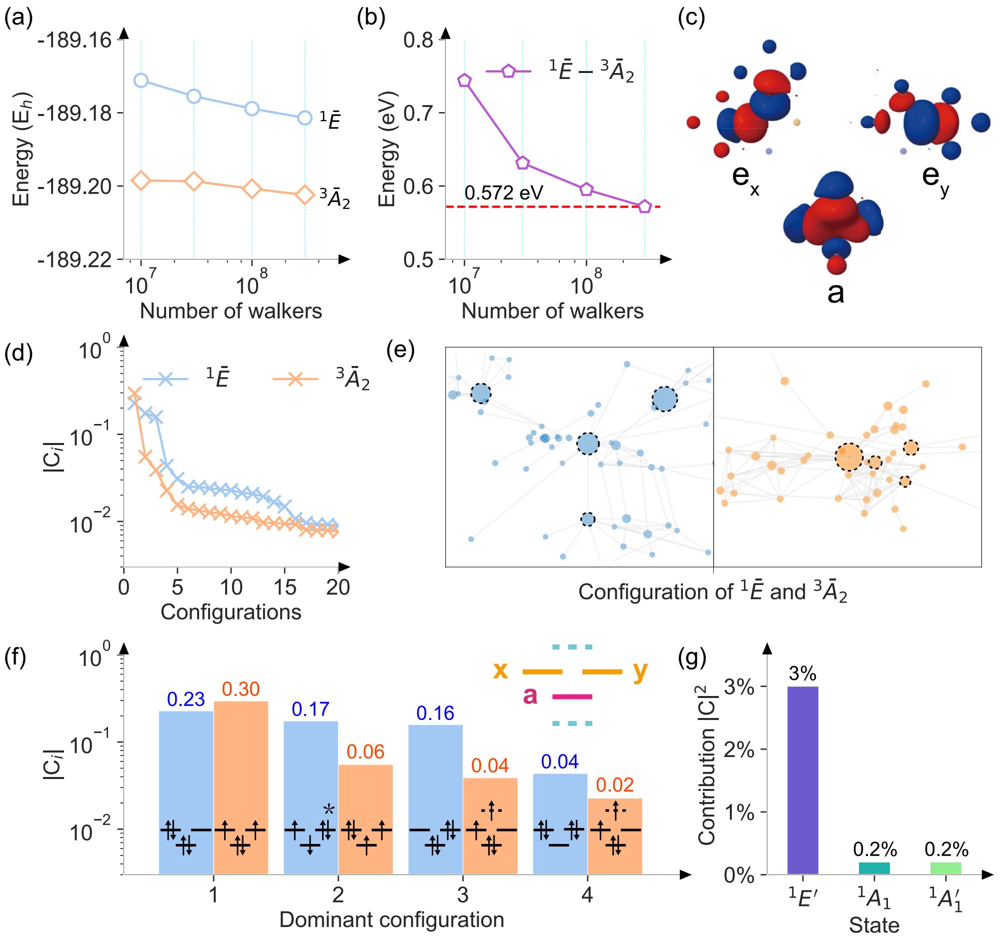

FIG. 3. FCIQMC calculations of NV^-. (a) The FCIQMC energies of $^1\bar{E}$ and $^3\bar{A}_2$ as a function of the number of walkers. (b) The corresponding excitation energies of $^1\bar{E} \leftrightarrow {}^3\bar{A}_2$. The red dashed line shows the final estimate at 0.572 eV. (c) Embedded frontier molecular orbitals $e_{x,y}$ and a_1. (d) The amplitude of the 20 most populated configurations from FCIQMC. (e) The configuration graphs of $^1\bar{E}$ (left) and $^3\bar{A}_2$ (right) states, characterizing the population and connection of configurations sampled from FCIQMC [38]. The size of each circle represents the absolute value of the CI coefficient, and the length of connecting lines correlates inversely with the transition matrix element between two configurations. The four most populated configurations have been highlighted by dashed lines. (f) The amplitude of the four most populated configurations of the spin triplet $^3\bar{A}_2$ (orange) and the singlet state $^1\bar{E}$ (blue). The corresponding configurations are described by frontier orbitals x, y, and a [solid lines in the inset, same as (c)], as well as orbitals with lower energies and higher energies (dashed lines in the inset), occupied by four spin electrons. The asterisk represents a normalized conjugate configuration. (g) In multiconfigurational electronic state $^1\bar{E}$, the contributions $|C|^2$ of three mixed-in single-configurational states $^1E'$, $^1A_1$, and $^1A_1'$. C represents the CI expansion coefficient corresponding to the single-configurational state.

(FCIQMC) methods, as displayed in SM Fig. S4. For both the total spin density distribution and the magnetization density distribution, the differences between the two methods are negligible, with the magnetization density distributed mainly around the three carbon atoms. The results also indicate that the mean-field approximation is qualitatively effective in describing the spatial density of electrons around the defect.

Next, we discuss the non-negligible multiconfigurational effects in NV^-. Firstly, it is essential to the intersystem crossing (ISC) transition, which can be observed in experiments. We use x, y, and a to refer to the corresponding configuration, and for the ground state $^3\bar{A}_2$ the most dominant configuration is $|a\bar{a}xy\rangle$. The second most populated configuration is $|a\bar{x}xy\rangle$, which accounts for 2% of $|a\bar{a}xy\rangle$. Due to orbital degeneracy, the single-configurational state ^1E is also doubly degenerate, written as $^1E_{x,y}$ [8]. $^1E_{x,y}$ and $^1A_1$ are expressed as follows:

$$
\begin{aligned}
|^1E_x\rangle &= \frac{1}{\sqrt{2}}(|a\bar{a}x\bar{x}\rangle - |a\bar{a}y\bar{y}\rangle),\\
|^1E_y\rangle &= \frac{1}{\sqrt{2}}(|a\bar{a}x\bar{y}\rangle - |a\bar{a}\bar{x}y\rangle),\\
|^1A_1\rangle &= \frac{1}{\sqrt{2}}(|a\bar{a}x\bar{x}\rangle + |a\bar{a}y\bar{y}\rangle). \qquad (15)
\end{aligned}
$$

TABLE I. The excitation energies (eV) of $^1\bar{E} \leftrightarrow {}^3\bar{A}_2$ and $^3\bar{E} \leftrightarrow {}^1\bar{A}_1$ in the negatively charged nitrogen vacancy (NV$^-$) obtained with different methods (also depicted in Fig. 4).

	Excitation (eV)	
Approach	$^1\bar{E} \leftrightarrow {}^3\bar{A}_2$	$^3\bar{E} \leftrightarrow {}^1\bar{A}_1$
FCIQMC-in-DFT	0.583	0.407[a]
Stochastic CI.[b]	0.629, 0.644	
DFT-cluster[c]	0.482	
Cluster Hubbard[d]	0.41	1.35
GW+BSE[e]	0.40	1.10
CI, CI-RPA, and CI-cRPA, respectively[f]	0.7, 0.476, 0.49	∼0.1, 0.545, 0.61
Variational quantum eigensolvers (VQEs)[g]	∼0.470–0.561	∼0.243–0.682
Extended Hubbard fit to GW[h]	∼0.5	∼0.6
Experiment		(∼0.344–0.430)[i]

[a] Combined with experiment in Refs. [32,40].
[b] $C_{42}H_{42}N^-$ results in Ref. [18].
[c] $C_{284}H_{144}N^-$ results in Ref. [18].
[d] An extended Hubbard cluster model of Ref. [17].
[e] Reference [16].
[f] Reference [19].
[g] References [20,39].
[h] An extended Hubbard model fitted to GW in Ref. [9].
[i] Estimated by Ref. [41] with a model for intersystem crossing.

In addition, the high-energy states with the *a* orbital not being fully occupied are also relevant, including $^1E'_{x,y}$ and $^1A_1{}'$:

$$|^1E'_x\rangle = \frac{1}{\sqrt{2}}(|a\bar{x}y\bar{y}\rangle - |\bar{a}xy\bar{y}\rangle),$$

$$|^1E'_y\rangle = \frac{1}{\sqrt{2}}(|a\bar{x}x\bar{y}\rangle - |\bar{a}x\bar{x}y\rangle),$$

$$|^{1'}A_1\rangle = |x\bar{x}y\bar{y}\rangle. \tag{16}$$

Combining the configuration population in Fig. 3(f) and Eqs. (15) and (16), the redefined mixed multideterminant singlet state $^1\bar{E}$ is a mixture of single-configurational states ^1E, $^1E'$, $^1A_1$, and $^1A_1{}'$. We noticed that $^3A_2$ is not linked to ^1E in the single-configuration picture [8], but it is linked to $^1E'$ and $^1A_1$ through spin-orbit coupling (SOC). Therefore it is highly likely that the occurrence of ISC between $^1\bar{E}$ and $^3\bar{A}_2$ in the experiment could be attributed to the influence of minor components present in $^1\bar{E}$ such as $^1A_1$ or $^1E'$. References [19] and [42] shed light on the potential roles of these components in ISC through different mechanisms. Referring to Ref. [19], it was demonstrated that the ^1E state can be split into ^1A and $^1A'$ when in low symmetry, suggesting a link between the ^1E state and the $m_S = \pm 1$ state of the ground state $^3A_2$ through the perpendicular component of SOC. Additionally,

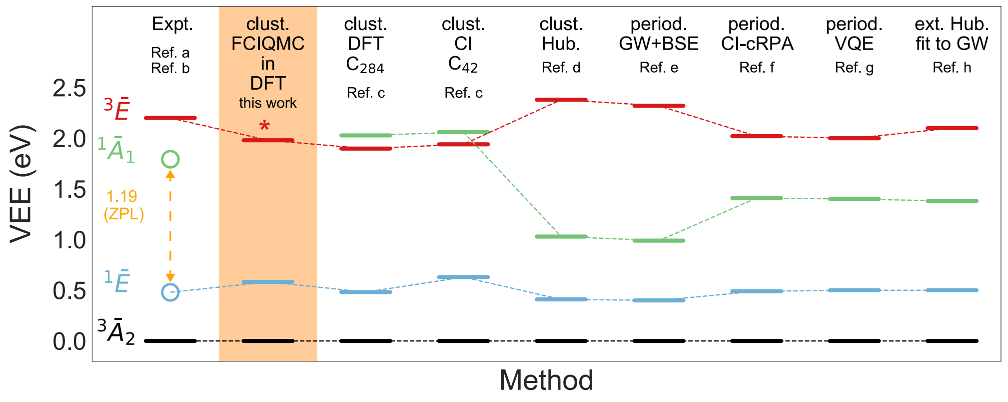

FIG. 4. Vertical excitation energies (VEEs) relative to the ground state $^3\bar{A}_2$ (0 eV) of excited states $^1\bar{E}$, $^1\bar{A}_1$, and $^3\bar{E}$ of NV$^-$. Here, clust., cluster model; ext. Hub., extended Hubbard model; Hub., Hubbard model; period., periodic model. The energy of $^3\bar{E}$ obtained in this paper (FCIQMC-in-DFT, highlighted in orange) is marked with an asterisk due to the influence of image states. Refs. a and b, Refs. [32] and [40] (experimental values: the VEE for $^3\bar{E} \leftrightarrow {}^3\bar{A}_2$ is 2.20 eV, and the zero phonon line (ZPL) is 1.945 eV [32]; the ZPL for $^1\bar{A}_1 \leftrightarrow {}^1\bar{E}$ is 1.19 eV [40]); Ref. c, Ref. [18] (DFT calculations of $C_{284}H_{144}N^-$ and stochastic CI of $C_{42}H_{42}N^-$); Ref. d, Ref. [17] (extended Hubbard cluster model); Ref. e, Ref. [16] (GW+BSE); Ref. f, Ref. [19] (CI-cRPA); Ref. g, Refs. [20,39] (variational quantum eigensolvers); Ref. h, Ref. [9] (extended Hubbard model fitted to GW).

the dominant determinant of $^1A_1$ is coupled with the $m_S = 0$ spin state of $^3A_2$ through the parallel component of SOC. Reference [42] suggested that mixing ^1E and $^1E'$ could facilitate a (Γ_z) ISC process between ^1E and $^3A_2^{\pm}$. Although our multiconfigurational electronic structure results fall short of fully explaining the specific mechanism of ISC, our results and analyses provide an additional perspective and evidence for understanding ISC.

Furthermore, it has been demonstrated that $^1E'$ can bring the dynamic Jahn-Teller (DJT) effect into $^1\bar{E}$ with a damped factor 0.01 [42], resulting in a split of the E-vibronic states in the photoluminescence spectrum of the singlets [40]. Previous theoretical analyses have discussed the DJT effect by assuming that the correlated electronic state $^1\bar{E}$ consists of ^1E and $^1E'$ [42]. The contribution of $^1E'$ (10% in Refs. [19,42]) to the dominant ^1E in $^1\bar{E}$ has been slightly overestimated. We estimate that, as Fig. 3(g) shows, the contribution of $^1E'$ is 3%. However, when considering the relative contribution (37%) of the lesser component $^1E'$ to the dominant component ^1E in a two-state component model of $^1\bar{E}$ (the same model as in Ref. [42]), we would get a larger DJT damped factor of 0.07. This implies a stronger DJT effect and explains the large splitting energies of the two E-vibronic states in experiments. Besides the DJT effect, the pseudo-Jahn-Teller (PJT) effect contributes to the electron-phonon interactions of the shelving singlet states in NV$^-$, which couple $^1\bar{A}_1$ and $^1\bar{E}$. In contrast to the enhanced contribution of the DJT effect, our results indicate that the PJT effect would be relatively less important than the previous prediction indicates [42]. We also notice the small relative contribution of $^1A_1$ (0.2%) in $^1\bar{E}$, which is consistent with previous theoretical analyses [7], along with a 0.2% contribution of $^1A_1{}'$. We expect the mixing of these high-energy states to induce new electron-phonon interactions that have not been considered in current theoretical models. Overall, the multiconfigurational nature of NV$^-$ states can be insightful for understanding the optical measurements, the electron-phonon interactions, and the spin selection mechanism in ISC, which are useful to improve spin initialization and readout in experiments.

3. Discussion on $^3\bar{E}$ *and* $^1\bar{A}_1$

In addition to the lowest-energy singlet and triplet states, using the multireplica technique of FCIQMC, we can also compute the excited $^3\bar{E}$ state. Figure 4 displays the vertical excitation energies (VEEs) of different excited states with respect to $^3\bar{A}_2$. The experimental values are shown in the first column. Overall, it can be observed that for the excited state $^3\bar{E}$ (shown in red), the VEEs calculated by these state-of-the-art methods are within 0.4 eV from the experimental value of 2.18 eV. In particular, we obtain a VEE of 1.98 eV, which lies close to other state-of-the-art calculations, which suggests the effectiveness of our embedding model.

It is also quite obvious that there is still a gap of approximately 0.2 eV between accurate theoretical calculations and the experimental estimation of VEE of $^3\bar{E}$, and the reason is not fully clear. As mentioned, in some calculations, the energy of the $^1\bar{A}_1$ state is even higher than that of the $^3\bar{E}$ state. Unfortunately, our FCIQMC-in-DFT calculation also suffers from this bias because this seems to be a general problem for finite cluster models. The most likely reason is the impact of so-called image states, which have been discussed in detail in Ref. [43]. The image states are generated because the peripheral C-H bonds would affect the conduction band (CB) edge and thereby affect the defect states in the band gap. We indeed observe electron transfer from the a_1 orbital to the lowest unoccupied molecular orbital (LUMO); hence the computed $^3\bar{E}$ state in FCIQMC-in-DFT is not a pure ^3E state ($a_1^{(1)}e_{x,y}^{(3)}$) because of the effect of the image states. So we marked it with an asterisk in Fig. 4.

The periodic embedding models can avoid such image states, and the results of these models may not suffer from the wrong energy ordering of the $^3\bar{E}$ and the $^1\bar{A}_1$ states; however, their results also deviate from the accepted experimental values. Specifically, the energies of the $^1\bar{A}_1$ state are usually too low inside the gap, as mentioned. Even for the level of the $^3\bar{E}$ state, the CI-cRPA calculation embedding in a periodic model gave a result of 2.02 eV [19], which is very similar to our FCIQMC-in-DFT calculation with a cluster model (1.98 eV). These results indicate the complexity of the electronic structure of the excited states, and it is fair to say that developing more accurate and efficient methods to describe the excited states of NV$^-$ still remains a challenge.

For the $^3\bar{E} \leftrightarrow {}^1\bar{A}_1$ ISC process, the results from different methods vary more significantly. For example, in Ref. [17], both the CI calculation based on the C$_{42}$ cluster and the DFT calculation based on the C$_{284}$ cluster yielded slightly higher energies for $^1\bar{A}_1$ than for $^3\bar{E}$, which is inconsistent with experiment. The calculations on a C$_{71}$ cluster based on the Hubbard model in Ref. [17] showed an overestimation of the $^3\bar{E} \leftrightarrow {}^1\bar{A}_1$ gap of 1.35 eV. Periodic models [9,16,19,20,39] did not yield a situation where the energy of $^1\bar{A}_1$ was higher than that of $^3\bar{E}$ but obtained results that varied within the large range 0.1–1.1 eV. Although there is still no direct measurement for $^3\bar{E} \leftrightarrow {}^1\bar{A}_1$, Ref. [41] estimated the range to be approximately 0.34–0.43 eV with a model for intersystem crossing. To provide a reasonable reference experimental value, we combined the precise $^1\bar{E} \leftrightarrow {}^3\bar{A}_2$ result of FCIQMC-in-DFT with the vertical excitation energy (VEE) of $^3\bar{E} \leftrightarrow {}^3\bar{A}_2$ and the zero-phonon line (ZPL) energy of $^1\bar{A}_1 \leftrightarrow {}^1\bar{E}$ in experiments [32,40] and obtained a reference value of 0.407 eV, which is consistent with Ref. [41]. Overall, the significant difference in the description of the energy gap for $^3\bar{E} \leftrightarrow {}^1\bar{A}_1$ between the cluster and periodic models highlights the complexity of the electronic states involved, calling for the further development of more accurate electronic structure methods.

B. Neutral and positively charged NV centers

Using the same embedding potential, we also perform the FCIQMC-in-DFT calculations for NV^0 and NV$^+$. Figure 5 plots the most populated configurations of ground states $^2\bar{E}$ (NV^0) and $^1\bar{A}_1$ (NV$^+$), as well as a spin triplet state of NV$^+$ labeled as $^3\bar{E}$. The multiconfigurational nature affects not only the electronic states, but also the charge density distribution in the vicinity of the NV defect. Reference [10] reported the experimental and DFT values for nuclear spin

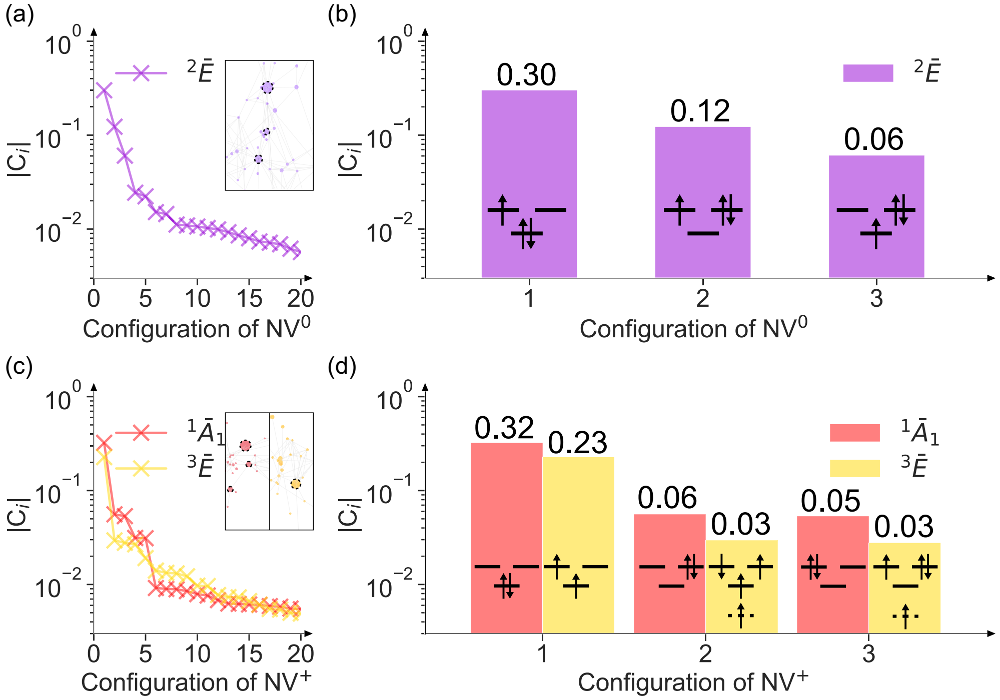

FIG. 5. Multiconfigurations of NV^0 and NV^+. (a) Amplitude of the 20 most populated configurations for the ground state $^2\bar{E}$ of NV^0. The inset shows the corresponding configuration graph. (b) The three dominating configurations for $^2\bar{E}$ of NV^0 with orbital occupation indicated. (c) and (d) Same as (a) and (b) for the ground state $^1\bar{A}_1$ and excited state $^3\bar{E}$ of NV^+.

quadrupole splitting $C_q = 3eQ_NV_{zz}/4h$ of ^{14}N for three NV centers at their ground states. The splitting is proportional to the electric field gradient V_{zz} at the nitrogen nucleus and the nuclear electric quadrupole moment Q_N. From NV^- via NV^0 to NV^+, electrons are preferentially excited from the $e_{x,y}$ orbitals, and the remaining electrons tend to increase their distance to the nitrogen nucleus, which leads to the reduction in V_{zz} and, consequently, the decrease in the absolute value of quadrupole splitting $|C_q|$. The experimental values of $|C_q|$ for NV^-, NV^0, and NV^+ are 4.945, 4.655, and 4.619 MHz, respectively. However, DFT calculations predicted a linear decrease in $|C_q|$ from NV^- to NV^0 to NV^+, which is inconsistent with experiments. The experimental values indicate that the charge density distribution in the vicinity of the nitrogen of NV^0 is closer to that of NV^+ than that of NV^-. The authors of Ref. [10] briefly mention that the ground state $^2\bar{E}$ of NV^0 is a correlated many-body state that cannot be accurately described by DFT (single configuration), which is consistent with our FCIQMC-in-DFT results. The electronic structure of $^2\bar{E}$ shows a strong multiconfigurational nature [Figs. 5(a) and 5(b)]. The authors of Ref. [10] also mention the existence of charge depletion on nitrogen atoms supported by a 5% population of the $a_1^{(1)}e_{x,y}^{(2)}$ configuration in $^2\bar{E}$. Our FCIQMC-in-DFT results confirm the mechanism and reveal the role of multiconfigurational correlation effects. Additionally, we found that not only on the ground state of NV^0 but also on those of NV^- and NV^+, the DFT-calculated absolute values are smaller than the experimental values, with a deviation of 0.075 MHz for NV^-, 0.265 MHz for NV^0, and 0.201 MHz for NV^+, respectively, as shown in $\Delta|C_q|$ [Fig. 6(c)]. These differences can also be attributed to the multiconfigurational nature of the corresponding states. Figure 5 shows the configuration occupation obtained by FCIQMC-in-DFT for states of NV^0 and NV^+. The ground states of the three charge states are $^3\bar{A}_2$ (NV^-), $^2\bar{E}$ (NV^0), and $^1\bar{A}_1$ (NV^+). The dominant configurations of the three states all have the a_1 orbital fully occupied, namely, $|a\bar{a}\bar{y}y\rangle$, $|a\bar{a}x\rangle$, and $|a\bar{a}\rangle$, respectively. The non-negligible components where the a_1 orbital is singly occupied or empty cause delocalization of the charge density distribution around nitrogen atoms and a reduction in $|C_q|$. We can divide the relevant configurations into three types: The a_1 orbital is fully occupied (type I), the a_1 orbital is singly occupied (type II), and the a_1 orbital is unoccupied (type III). Then we can compute the relative contribution of the type II and type III configurations [RC, defined in Fig. 6(a)], and we find that the ground state $^3\bar{A}_2$ of NV^- has a relative contribution of 2%, whereas $^2\bar{E}$ of NV^0 has 18% and $^1\bar{A}_1$ of NV^+ has 6%. The relative contribution qualitatively explains the trend of the depletion of charge density distribution at the nitrogen atom, which is measured by $|C_q|$ in Fig. 6(c).

We also calculate the natural atomic orbital (NAO) occupancy of the a-type orbital of the three ground states [Fig. 6(b)]. For $^3A_2$ of NV^-, the natural occupancy is 1.956, in which the tiny depletion (compared with 2) results in a small decrease in $|C_q|$. The natural occupancy decreases to 1.785 for NV^0, indicating that the ionization process from NV^- to NV^0 significantly affects the electric field near the nitrogen vicinity. For NV^+, the natural occupancy is 1.818, and its charge distribution depletion degree is between NV^- and NV^0. Figure 6(c) plots the natural occupancy depletion in the a orbital ($\Delta|O_a|$) for the three charged NV centers. The trend is consistent with $\Delta|C_q|$, which is defined as the

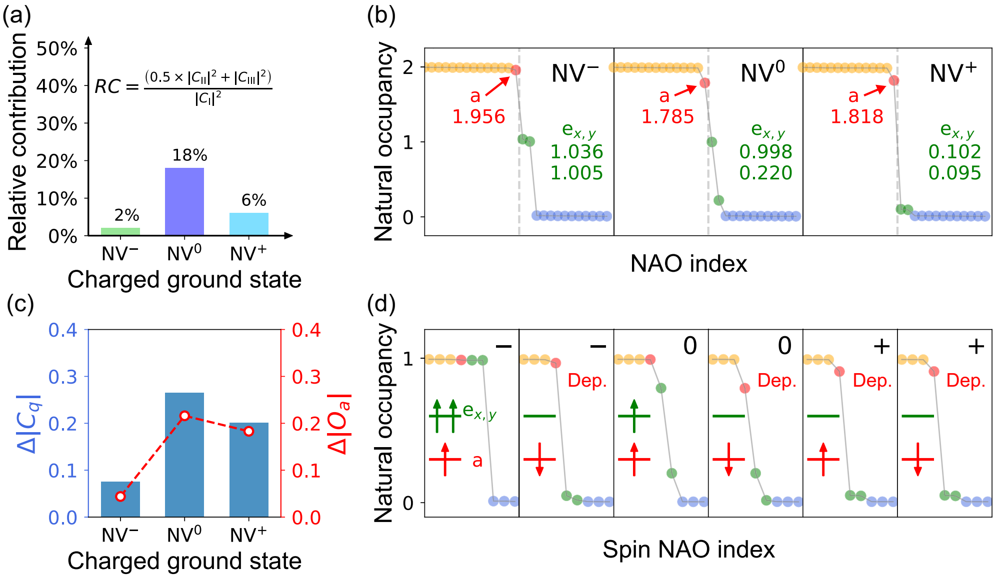

FIG. 6. Calculations on different charge states of NV centers. (a) For the ground states ${}^3\bar{A}_2$, ${}^2\bar{E}$, and ${}^1\bar{A}_1$ of the three charged NV centers, the relative contribution of the sum of the type II and type III configurations with respect to the type I configuration (the first three most populated configurations only involving the x, y, and a orbitals). The coefficient 0.5 in the definition of the relative contribution (RC) results from the assumption that the depletion contribution of type II is half that of type III. (b) Total natural occupancy (spin up plus spin down) for the ground states of the three charged NV centers. Red points highlight the natural atomic orbital (NAO) occupancy corresponding to the a orbital. (c) The blue histogram (left axis) shows the difference between the experimental and DFT-calculated values for nuclear spin quadrupole splittings ($\Delta|C_q|$ in units of MHz) via data reported in Ref. [10]. The red dashed line (right axis) shows the natural occupancy depletion of a ($\Delta|O_a|$) calculated from FCIQMC. (d) The NAO occupancy of the spin-majority channel (spin up, left) and the spin-minority channel (spin down, right) of three charged ground states [same as (b)]. Dep., the spin channel of main charge depletion.

difference in experimentally measured and DFT-calculated values of the nuclear spin quadrupole splitting [10].

Furthermore, we can analyze the spin channels of the NAO [Fig. 6(d)]. For NV$^-$, this analysis clearly shows that the single-particle states in the spin-minority (spin-down) channel are mostly responsible for the electron excitation from the a_1 to the $e_{x,y}$ orbitals and the corresponding excitation of ${}^3\bar{E} \leftrightarrow {}^3\bar{A}_2$, which is consistent with Ref. [43]. A more interesting observation is that, in addition to the same two spin channels as in the NV$^+$center, charge depletions in both the NV$^-$ center and the NV^0 center primarily occur in the spin-minority channel (labeled “Dep.” in the figure). Since the spin-minority channel is more likely to exhibit electron excitation from the a_1 to the $e_{x,y}$ orbitals, this suggests a possible positive correlation between electron excitation and charge depletion. This phenomenon may provide valuable insights into the microscopic processes underlying charge-state transitions in NV centers and warrants further investigation through more accurate electronic structure studies.

IV. CONCLUSION

To conclude, in this paper we have integrated the FCIQMC methods with DMFET to achieve accurate *ab initio* calculations of NV centers in diamond. Our results provide a benchmark for the quantum states that are still a subject of uncertainty in experimental and theoretical studies. The revealed multiconfigurational nature of the quantum states in NV centers offers insights that can assist our understanding of sophisticated experiments in the laboratory, which may further guide the optimization of photoelectronic quantum processes and lead to improved theoretical models. With continuous developments of FCIQMC and embedding theory, the computational framework of this study will allow us to tackle more complex quantum states in solids and defects in semiconductors, working systematically towards the exact solution, providing valuable theoretical insights.

ACKNOWLEDGMENTS

The authors thank Wei Fang for sharing a PYTHON wrap for geometry optimization and thank Gangqin Liu for helpful discussions. This work was supported by the National Natural Science Foundation of China under Grants No. 92165101 and No. 11888101 and the Strategic Priority Research Program of the Chinese Academy of Sciences under Grant No. XDB33000000. We are grateful for computational resources provided by the TianHe-1A supercomputer, the High Performance Computing Platform of Peking University, and the Platform for Data Driven Computational Materials Discovery of the Songshan Lake Materials Laboratory.

[1] J. R. Weber, W. F. Koehl, J. B. Varley, A. Janotti, B. B. Buckley, C. G. Van de Walle, and D. D. Awschalom, Quantum computing with defects, Proc. Natl. Acad. Sci. USA **107**, 8513 (2010).

[2] C. E. Dreyer, A. Alkauskas, J. L. Lyons, A. Janotti, and C. G. Van de Walle, First-principles calculations of point defects for quantum technologies, Annu. Rev. Mater. Res. **48**, 1 (2018).

[3] F. Dolde, I. Jakobi, B. Naydenov, N. Zhao, S. Pezzagna, C. Trautmann, J. Meijer, P. Neumann, F. Jelezko, and J. Wrachtrup, Room-temperature entanglement between single defect spins in diamond, Nat. Phys. **9**, 139 (2013).

[4] G. Waldherr, Y. Wang, S. Zaiser, M. Jamali, T. Schulte-Herbrüggen, H. Abe, T. Ohshima, J. Isoya, J. F. Du, P. Neumann, and J. Wrachtrup, Quantum error correction in a solid-state hybrid spin register, Nature (London) **506**, 204 (2014).

[5] G.-Q. Liu, Y.-R. Zhang, Y.-C. Chang, J.-D. Yue, H. Fan, and X.-Y. Pan, Demonstration of entanglement-enhanced phase estimation in solid, Nat. Commun. **6**, 6726 (2015).

[6] S. Zaiser, T. Rendler, I. Jakobi, T. Wolf, S.-Y. Lee, S. Wagner, V. Bergholm, T. Schulte-Herbrüggen, P. Neumann, and J. Wrachtrup, Enhancing quantum sensing sensitivity by a quantum memory, Nat. Commun. **7**, 12279 (2016).

[7] Á. Gali, *Ab initio* theory of the nitrogen-vacancy center in diamond, Nanophotonics **8**, 1907 (2019).

[8] M. W. Doherty, N. B. Manson, P. Delaney, and L. C. L. Hollenberg, The negatively charged nitrogen-vacancy centre in diamond: the electronic solution, New J. Phys. **13**, 025019 (2011).

[9] S. Choi, M. Jain, and S. G. Louie, Mechanism for optical initialization of spin in NV$^-$ center in diamond, Phys. Rev. B **86**, 041202(R) (2012).

[10] M. Pfender, N. Aslam, P. Simon, D. Antonov, G. Thiering, S. Burk, F. Fávaro de Oliveira, A. Denisenko, H. Fedder, J. Meijer, J. A. Garrido, A. Gali, T. Teraji, J. Isoya, M. W. Doherty, A. Alkauskas, A. Gallo, A. Grüneis, P. Neumann, and J. Wrachtrup, Protecting a diamond quantum memory by charge state control, Nano Lett. **17**, 5931 (2017).

[11] S. Pezzagna and J. Meijer, Quantum computer based on color centers in diamond, Appl. Phys. Rev. **8**, 011308 (2021).

[12] W. Zheng, K. Bian, X. Chen, Y. Shen, S. Zhang, R. Stöhr, A. Denisenko, J. Wrachtrup, S. Yang, and Y. Jiang, Coherence enhancement of solid-state qubits by local manipulation of the electron spin bath, Nat. Phys. **18**, 1317 (2022).

[13] A. Gali, M. Fyta, and E. Kaxiras, *Ab initio* supercell calculations on nitrogen-vacancy center in diamond: Electronic structure and hyperfine tensors, Phys. Rev. B **77**, 155206 (2008).

[14] J. A. Larsson and P. Delaney, Electronic structure of the nitrogen-vacancy center in diamond from first-principles theory, Phys. Rev. B **77**, 165201 (2008).

[15] G. H. Booth, A. Grüneis, G. Kresse, and A. Alavi, Towards an exact description of electronic wavefunctions in real solids, Nature (London) **493**, 365 (2013).

[16] Y. Ma, M. Rohlfing, and A. Gali, Excited states of the negatively charged nitrogen-vacancy color center in diamond, Phys. Rev. B **81**, 041204(R) (2010).

[17] A. Ranjbar, M. Babamoradi, M. H. Saani, M. A. Vesaghi, K. Esfarjani, and Y. Kawazoe, Many-electron states of nitrogen-vacancy centers in diamond and spin density calculations, Phys. Rev. B **84**, 165212 (2011).

[18] P. Delaney, J. C. Greer, and J. A. Larsson, Spin-polarization mechanisms of the nitrogen-vacancy center in diamond, Nano Lett. **10**, 610 (2010).

[19] M. Bockstedte, F. Schütz, T. Garratt, V. Ivády, and A. Gali, Ab initio description of highly correlated states in defects for realizing quantum bits, npj Quantum Mater. **3**, 31 (2018).

[20] H. Ma, M. Govoni, and G. Galli, Quantum simulations of materials on near-term quantum computers, npj Comput. Mater. **6**, 85 (2020).

[21] G. H. Booth, A. J. W. Thom, and A. Alavi, Fermion Monte Carlo without fixed nodes: A game of life, death, and annihilation in slater determinant space, J. Chem. Phys. **131**, 054106 (2009).

[22] K. Guther, R. J. Anderson, N. S. Blunt, N. A. Bogdanov, D. Cleland, N. Dattani, W. Dobrautz, K. Ghanem, P. Jeszenszki, N. Liebermann, G. L. Manni, A. Y. Lozovoi, H. Luo, D. Ma, F. Merz, C. Overy, M. Rampp, P. K. Samanta, L. R. Schwarz, J. J. Shepherd *et al.*, NECI: N-electron configuration interaction with an emphasis on state-of-the-art stochastic methods, J. Chem. Phys. **153**, 034107 (2020).

[23] N. A. Bogdanov, G. Li Manni, S. Sharma, O. Gunnarsson, and A. Alavi, Enhancement of superexchange due to synergetic breathing and hopping in corner-sharing cuprates, Nat. Phys. **18**, 190 (2022).

[24] K. Yu and E. A. Carter, Extending density functional embedding theory for covalently bonded systems, Proc. Natl. Acad. Sci. USA **114**, E10861 (2017).

[25] X. Zhang and E. A. Carter, Subspace density matrix functional embedding theory: Theory, implementation, and applications to molecular systems, J. Chem. Theory Comput. **15**, 949 (2019).

[26] J. P. Goss, R. Jones, S. J. Breuer, P. R. Briddon, and S. Öberg, The Twelve-Line 1.682 eV Luminescence Center in Diamond and the Vacancy-Silicon Complex, Phys. Rev. Lett. **77**, 3041 (1996).

[27] See Supplemental Material at http://link.aps.org/supplemental/10.1103/PhysRevB.108.045111 for supporting information, including additional references [28–32].

[28] F. R. Petruzielo, A. A. Holmes, H. J. Changlani, M. P. Nightingale, and C. J. Umrigar, Semistochastic Projector Monte Carlo Method, Phys. Rev. Lett. **109**, 230201 (2012).

[29] N. S. Blunt, S. D. Smart, J. A. F. Kersten, J. S. Spencer, G. H. Booth, and A. Alavi, Semi-stochastic full configuration interaction quantum Monte Carlo: Developments and application, J. Chem. Phys. **142**, 184107 (2015).

[30] Q. Sun, T. C. Berkelbach, N. S. Blunt, G. H. Booth, S. Guo, Z. Li, J. Liu, J. D. McClain, E. R. Sayfutyarova, S. Sharma, S. Wouters, and G. K.-L. Chan, PySCF: the Python-based simulations of chemistry framework, Wiley Interdiscip. Rev.: Comput. Mol. Sci. **8**, e1340 (2018).

[31] Á. Gali, E. Janzén, P. Deák, G. Kresse, and E. Kaxiras, Theory of Spin-Conserving Excitation of the $N-V^-$ Center in Diamond, Phys. Rev. Lett. **103**, 186404 (2009).

[32] G. Davies and M. F. Hamer, Optical studies of the 1.945 eV vibronic band in diamond, Proc. R. Soc. London Ser. A **348**, 285 (1976).

[33] F. R. Manby, M. Stella, J. D. Goodpaster, and T. F. Miller, A simple, exact density-functional-theory embedding scheme, J. Chem. Theory Comput. **8**, 2564 (2012).

[34] R. W. Warren and B. I. Dunlap, Fractional occupation numbers and density functional energy gradients within the linear

combination of Gaussian-type orbitals approach, Chem. Phys. Lett. **262**, 384 (1996).

[35] D. Cleland, G. H. Booth, and A. Alavi, Communications: Survival of the fittest: Accelerating convergence in full configuration-interaction quantum Monte Carlo, J. Chem. Phys. **132**, 041103 (2010).

[36] K. Ghanem, A. Y. Lozovoi, and A. Alavi, Unbiasing the initiator approximation in full configuration interaction quantum Monte Carlo, J. Chem. Phys. **151**, 224108 (2019).

[37] K. Ghanem, K. Guther, and A. Alavi, The adaptive shift method in full configuration interaction quantum Monte Carlo: Development and applications, J. Chem. Phys. **153**, 224115 (2020).

[38] L. Sun, Z. Zhang, T. Jiang, Y. Chen, and J. Chen, Graphic characterization and clustering configuration descriptors of determinant space for molecules, J. Chem. Theory Comput. **19**, 2282 (2023).

[39] B. Huang, M. Govoni, and G. Galli, Simulating the Electronic Structure of Spin Defects on Quantum Computers, PRX Quantum **3**, 010339 (2022).

[40] L. J. Rogers, S. Armstrong, M. J. Sellars, and N. B. Manson, Infrared emission of the NV centre in diamond: Zeeman and uniaxial stress studies, New J. Phys. **10**, 103024 (2008).

[41] M. L. Goldman, A. Sipahigil, M. W. Doherty, N. Y. Yao, S. D. Bennett, M. Markham, D. J. Twitchen, N. B. Manson, A. Kubanek, and M. D. Lukin, Phonon-Induced Population Dynamics and Intersystem Crossing in Nitrogen-Vacancy Centers, Phys. Rev. Lett. **114**, 145502 (2015).

[42] G. Thiering and A. Gali, Theory of the optical spin-polarization loop of the nitrogen-vacancy center in diamond, Phys. Rev. B **98**, 085207 (2018).

[43] M. Kaviani, P. Deák, B. Aradi, T. Frauenheim, J.-P. Chou, and A. Gali, Proper surface termination for luminescent near-surface NV centers in diamond, Nano Lett. **14**, 4772 (2014).